Journal of Materials Chemistry A

ROYAL SOCIETY OF CHEMISTRY

PAPER

View Article Online
View Journal | View Issue

Check for updates

Cite this: J. Mater. Chem. A, 2025, 13, 3619

Stable functional electrode–electrolyte interface formed by multivalent cation additives in lithium-metal anode batteries†

Hongyi Li, *[a] Daichi Shimizu,[a] Rongkang Jin,[a] Tongqing Zhang,[a] Daisuke Horikawa,[b] Katsuhiko Nagaya,[b] Hiroshi Tsubouchi,[b] Hiroyuki Yamaguchi,[b] Motoyoshi Okumura[b] and Tetsu Ichitsubo *[a]

Li-metal anodes face challenges in terms of cyclability due to non-uniform deposition morphology and progressive electrolyte decomposition. Here, we discover the effects of multivalent cation salts (Ca^{2+}, Ba^{2+}, La^{3+}, Ce^{3+}) as electrolyte additives for Li-metal anodes in exemplary $[TFSI]^-$/EC–PC electrolytes. These additives induce strong Coulomb interactions that alter the solvation environment in the electrolyte, promoting the direct coordination of cations with $[TFSI]^-$. This modification of the solvation structure increases the desolvation energy, effectively slowing down the Li^+ depletion at the electrode surface and flattening the deposition morphology. Besides, the coordinated $[TFSI]^-$ tends to participate in the formation of the solid-electrolyte interphase (SEI), increasing the fluoride concentration ratio. Furthermore, these multivalent cations are also incorporated into the SEI and play an important role in its formation. In particular, the lanthanide additives form La–O and La–F bonds instead of Li-related bonds, which would effectively improve the uniformity and stability of the SEI, enabling the reversible formation of a flat and dense Li metal layer on the Cu foil current collector. In addition, full-cell tests with $LiFePO_4$ cathodes show that the lanthanide additives mitigate the internal resistance increase on Li metal anodes during cycling and drastically improve capacity retention in either "anode-free" or excess Li configurations.

Received 22nd October 2024
Accepted 18th December 2024

DOI: 10.1039/d4ta07531e

rsc.li/materials-a

Introduction

Alkali metals, such as Li and Na, have a low redox potential and a high theoretical capacity. These properties make them ideal candidates for anode materials.[1] However, their practical applications have been hampered by the major challenge of insufficient reversibility during repeated electrodeposition and dissolution processes.[2] In particular, during electrodeposition, the alkali cations are rapidly reduced to metal atoms and depleted near the electrode surface, creating a steep concentration gradient that drives the fatal dendritic growth.[3] The weakly bound dendrites easily lose electrical contact with the current collector, resulting in capacity loss and short circuit risk.[4] In addition, the solid-electrolyte interphase (SEI), formed from the cathodic decomposition products of the electrolyte species, usually lacks uniformity and rigidity.[5] As a result, the SEI is easily cracked, exposing fresh alkali metal deposits to the electrolyte, leading to progressive electrolyte decomposition and gradual capacity loss during cycling.

Therefore, to achieve ideal reversible alkali metal anodes, several challenges must be overcome: (i) ensuring a uniform and dense deposition morphology without dendrites, and (ii) establishing a chemically and structurally stable SEI to prevent the excess electrolyte decomposition. In recent years, considerable efforts have been made to improve the reversibility of alkali metal anodes though advanced design of the electrolyte and the electrode–electrolyte interface.[6–11] High concentration electrolytes (HCEs), also known as salt-concentrated or solvent-in-salt electrolytes,[12,13] have been reported as effective strategies to avoid dendritic formation. With appropriate salt-solvent combinations, increasing the salt concentration significantly retards the cation depletion during electrodeposition, thus avoiding the dendritic growth within the areal capacity load for commercial batteries (2–4 mA h cm^{-2}).[3] Moreover, HCEs usually show a markedly different solvation environment compared to the conventional dilute electrolytes, as illustrated in Fig. 1a and b. For the dilute electrolytes, such as 1 M $LiPF_6$ in EC–DMC (EC: ethylene carbonate, DMC: dimethyl carbonate, volume ratio 1 : 1), the salts are basically dissociated with the solvents forming solvent-separated ion pairs (SSIPs).[14] In contrast, for HCEs, such as 4 M Li[FSI] in DME ($[FSI]^-$: bis(fluorosulfonyl)imide, DME: 1,2-dimethoxyethane),[15] the salt dissociation is basically

[a]Institute for Materials Research, Tohoku University, Sendai 980-8577, Japan. E-mail: li.hongyi@tohoku.ac.jp; tichi@tohoku.ac.jp

[b]Advanced Battery Development Division, Toyota Motor Corporation, Toyota 471-8571, Japan

† Electronic supplementary information (ESI) available. See DOI: https://doi.org/10.1039/d4ta07531e

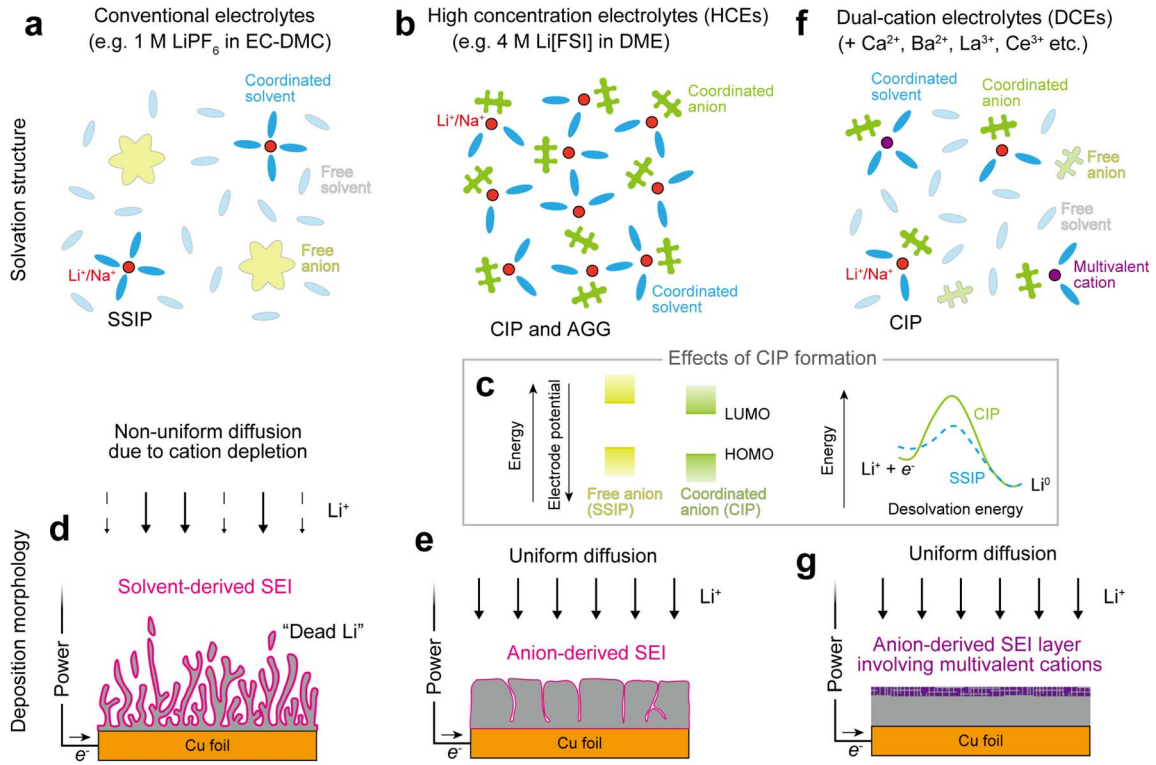

Fig. 1 Schematic illustration of the solvation environment and deposition morphology in different electrolytes for rechargeable Li batteries. (a) Solvation structure in conventional dilute electrolytes for Li-ion batteries. The cations are basically coordinated by solvent molecules as solvent-separated ion pairs (SSIPs). (b) Solvation structure in high concentration electrolytes (HCEs). The cations and anions keep a direct coordination as contact-ion pairs (CIPs) and aggregates (AGGs). (c) Effects of the CIP formation. The lowest unoccupied molecular orbital (LUMO) energy level of the anions is decreased in CIPs compared to the SSIPs (left). Besides, the strong solvation bonding of CIPs increases the activation energy for the desolvation in electrodeposition (right). (d) Deposition morphology in conventional dilute electrolytes. The Li^+ cations are rapidly consumed at the electrode surface, resulting to a mossy or dendritic morphology. (e) Deposition morphology in HCEs. Increasing the salt concentration and the corresponding CIP formation retard the cation depletion and maintain a flat and non-dendritic morphology. (f) Solvation structure in dual-cation electrolytes (DCEs). The CIP formation is promoted by the strong Coulomb interaction of the multivalent cation additives. (g) Deposition morphology in DCEs. The CIP formation retards the cation depletion on the electrode surface and maintains a flat deposition morphology. In addition, the multivalent cation additives are involved in the anion-derived SEI formation, which can be used as an effective factor to improve the interfacial stability on the Li metal anodes.

insufficient due to the limited number of solvent molecules, leading to the formation of a high ratio of contact-ion pairs (CIPs) and aggregates (AGGs) in HCEs.[13] The direct coordination of anions to cations reduces the lowest unoccupied molecular orbital (LUMO) and highest occupied molecular orbital (HOMO) energy levels compared to anions in SSIPs,[16] as shown on the left in Fig. 1c. As a result, the cathodic decomposition of anions in the SEI formation is promoted instead of the solvent. As illustrated in Fig. 1d and e, the anion-derived SEI formed in HCEs is empirically more stable than the solvent-derived SEI formed in conventional dilute electrolytes, accompanied by a higher ratio of LiF.[17] Besides, the CIPs and AGGs usually have a higher binding energy than the SSIPs as shown on the right in Fig. 1c. The higher binding energy results in a higher activation energy for desolvation, which also helps to retard the cation depletion during electrodeposition. Owing to these features, HCEs enable a flat and dense electrodeposition morphology with stable SEI, achieving a very high coulombic efficiency (around 99%) of Li deposition and dissolution. However, there are several limitations to the practical application of HCEs. HCEs tend to have high viscosity, which causes wettability problems on separators and electrodes. In addition, the salts are much more expensive than the solvents, which significantly increases the production costs. Therefore, attempts have been made to maintain a solvation environment similar to HCEs while reducing salt concentrations. Previous studies have shown that the introduction of non-solvating cosolvents can reduce SSIPs and increase CIPs and AGGs in the low concentration range.[18] These electrolytes are usually referred to as localized high concentration electrolytes (LHCEs).[19,20]

As an alternative strategy to improve the electrolytes for alkali-metal anodes, we have proposed a concept of dual-cation electrolytes (DCEs),[16] in which multivalent salts are introduced as electrolyte additives. The strong Coulomb interaction of the multivalent cations, such as Ca^{2+}, Ba^{2+}, La^{3+}, Ce^{3+}, usually causes strong solvation in electrolytes and poor ionic conductivity in SEI.[21] As a result, the multivalent cations are difficult to reduce to the metal state in organic electrolytes. These properties make multivalent cations suitable as electrolyte additives

for alkali-metal anodes. Previously, we have shown the effects of mixing alkaline earth cations (Ca^{2+}, Ba^{2+}) as electrolyte additives for Li and Na metal anodes with $[TFSI]^-$/G3 electrolytes ($[TFSI]^-$: bis(trifluoromethanesulfonyl)imide and G3: triethylene glycol dimethyl ether).[16] The experimental and computational results showed that the introduction of divalent cations modified the solvation environment in the electrolyte. Specifically, Li^+ and Na^+ were promoted to form CIPs instead of SSIPs (Fig. 1f) in order to mitigate the strong Coulomb interaction between the divalent cations and consequently reduce the free energy of the electrolyte system. As shown in Fig. 1g, the increase in CIPs contributes to the anion-derived SEI formation and dendrite-free morphology in Li and Na electrodeposition, which is similar to the phenomena observed in HCEs and LHCEs. More importantly, the multivalent cations are involved in the SEI formation, which is a unique feature of DCEs and provides a new factor to control the stability and functionality of SEI. In general, the SEI on Li metal anodes must have sufficient Li^+ conductivity as well as blocking electron conduction from the current collector to the electrolyte to prevent the excess electrolyte decomposition. Besides, the SEI must be robust enough to withstand the large volume changes associated with repeated Li deposition and dissolution. The multivalent cations have different charges, ionic radii, coordination numbers, and Madelung energies in forming ionic crystals, which would significantly affect the composition and mechanical properties of the SEI. In addition to Li metal anodes, similar effects have also been reported in improving the performance of Si anodes,[22] which suggests the versatile applications of the dual-cation strategies.

To reveal the mechanism of the multivalent cation additives, in this study, we employed different multivalent salts ($Ca[TFSI]_2$, $Ba[TFSI]_2$ and $La[TFSI]_3$, $Ce[TFSI]_3$) as additives in Li [TFSI]/EC–PC electrolyte (EC: ethylene carbonate, PC: propylene carbonate, volume ratio 1 : 1). The $[TFSI]^-$ salts are available in a wide variety of cations. This can simplify the comparison and avoid the complicated effects of mixing different anions. The mixed carbonate solvents combine a good stability and high polarity to dissolve the various multivalent salts, facilitating the control experiments. Compared to the alkaline earth elements, the lanthanide cations are basically in the trivalent state, which would be more effective in modifying the solvation structure. Besides, the lanthanides are key elements in Li super ionic conductors such as LLTO ($Li_{3x}La_{(2/3)-x}TiO_3$)[23] and LLZO ($Li_7La_3Zr_2O_{12}$).[24] Thus, the lanthanides would be favourable for improving the SEI functionality. In cycle tests of Cu||Li half cells, the addition of La^{3+} and Ce^{3+} markedly improved the coulombic efficiency of Li deposition/dissolution compared to the electrolyte containing only Li^+. In contrast, the Ca^{2+} and Ba^{2+} decreased the coulombic efficiency and significantly increased the overpotential, suggesting the passivation of the deposits. The constant current electrodeposition experiments with Cu||Li half cells confirmed that the multivalent cation additives (Ca^{2+}, La^{3+}) flattened the Li deposition morphology in initial cycles and these additives were not reduced to the metallic state. Moreover, with repeated deposition and dissolution, the Li deposits progressively accumulated and increased in thickness and porosity during cycling in the electrolyte containing only Li salt. In contrast, the addition of La salt helped to maintain a flat and dense Li metal layer that was reversibly formed on the current collector with little changes in thickness during cycling. Chemical analysis showed that the addition of La salt increased the fluoride ratio in SEI and helped to maintain a relatively stable SEI composition during repeated Li deposition and dissolution. The X-ray photoelectron spectroscopy (XPS) profiles showed that La–O and La–F bonds were formed in the SEI, which would help to improve the stability of the SEI. The experimental Raman spectroscopy, nuclear magnetic resonance (NMR) spectroscopy and computer simulation results confirmed that both the Li^+ and La^{3+} were promoted to form CIPs. The increase of CIPs would be the origin of the flat deposition morphology and the increase of the fluoride ratio in SEI. Finally, full-cell tests with $LiFePO_4$ cathodes showed that the La salt additives significantly improved the coulombic efficiency and capacity retention in "anode-free" or excess Li cell configurations. The electrochemical impedance spectroscopy (EIS) results further revealed that the La salt additive significantly mitigate the increase in interfacial resistance on Li metal anodes during cycling. The introduction of multivalent cations would be a promising strategy to improve the interfacial stability and the reversibility of alkali metal anodes.

Results and discussion

Li deposition/dissolution reversibility

To compare the effects of multivalent cation additives on Li-metal anodes, cycle tests were first carried out in Cu||Li half cells. For the electrolytes, 0.5 M Li[TFSI] in EC–PC (volume ratio 1 : 1) was used as the base electrolyte. For the multivalent salts ($Ca[TFSI]_2$, $Ba[TFSI]_2$, $La[TFSI]_3$ and $Ce[TFSI]_3$), the concentration was basically set to 0.1 M to facilitate the comparison. In two-electrode coin cells, a 20 μm-thick Cu foil was used as the working electrode (WE), and a 100 μm-thick Li foil (areal capacity about 20 mA h cm^{-2}) was used as the counter electrode (CE) and the reference electrode (RE). A surfactant-coated monolayer microporous membrane (Celgard #3501) was used as the separator. Fig. S1a in the ESI† shows the structure of the coin cell. During cycle tests, Li deposition was carried out until the areal capacity reached 2 mA h cm^{-2}. Li dissolution was then conducted until the cell voltage reached the cut-off voltage of 1 V. The current density was 1 mA cm^{-2}.

Fig. 2a compares the areal capacity of Li deposition/dissolution in the Cu||Li coin cells up to 10 cycles. As the deposition capacity was a fixed value in each cycle, the dissolution capacity was proportional to the coulombic efficiency. The coulombic efficiency in 0.5 M Li[TFSI]/EC–PC (hereafter referred to as "the Li electrolyte") gradually increased from about 80% in the first cycle to about 90% after ten cycles (dashed red line). The addition of the alkali earth salts ($Ca[TFSI]_2$, $Ba[TFSI]_2$) and the lanthanide salts ($La[TFSI]_3$, $Ce[TFSI]_3$) resulted in distinctively different effects. In 0.5 M Li [TFSI]–0.1 M $Ca[TFSI]_2$/EC–PC and 0.5 M Li[TFSI]–0.1 M Ba $[TFSI]_2$/EC–PC (abbreviated as "the Li–Ca electrolyte" and "the

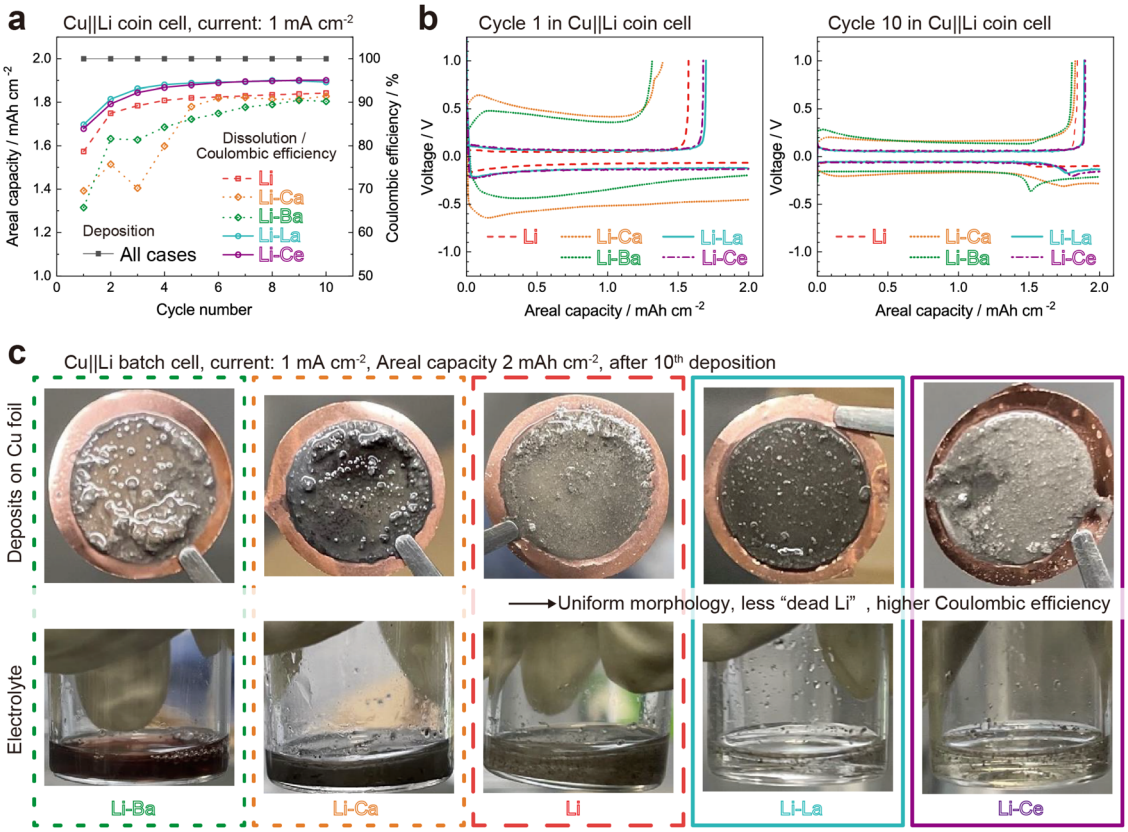

Fig. 2 Li deposition/dissolution behaviour in Cu||Li half cells with different $[TFSI]^-$/EC–PC electrolytes. The concentrations of Li[TFSI] and each multivalent cation salt were 0.5 M and 0.1 M, respectively. (a) Areal capacity of Li deposition and dissolution in cycle tests in two-electrode Cu||Li coin cells. The current density was 1 mA cm^{-2}. The deposition capacity was fixed to 2 mA h cm^{-2} in each cycle and thus the dissolution capacity also indicated the coulombic efficiency. The La^{3+} and Ce^{3+} additives markedly improved the coulombic efficiency of the Li deposition/dissolution, whereas the Ca^{2+} and Ba^{2+} decreased the coulombic efficiency. (b) Voltage profiles in the 1st cycle (left) and the 10th cycle (right) of the half cells. The La^{3+} and Ce^{3+} additives maintained a low overpotential and increased the dissolution capacity, while the Ca^{2+} and Ba^{2+} additives increased the overpotential and decreased the dissolution capacity. (c) Photos of Cu foil electrodes (upper) and electrolytes (lower) removed from three-electrode Cu||Li batch cells after 10th Li deposition. The current density was 1 mA cm^{-2} and the deposition capacity was fixed to 2 mA h cm^{-2}. The La^{3+} and Ce^{3+} additives significantly flattened the deposition morphology, decreased the floating Li deposits (known as "dead Li") peeling off from the Cu foil electrodes, and thereby improved the coulombic efficiency. The structures of two-electrode coin cells and three-electrode batch cells are shown in Fig. S1 in the ESI.†

Li–Ba electrolyte", *etc.*), the coulombic efficiencies increased from about 70% in the first cycle to about 90% after ten cycles (dotted orange and green lines), lower than the results in the Li electrolyte. In contrast, the coulombic efficiencies in the Li–La and Li–Ce electrolytes increased from 85% in the first cycle to 95% after ten cycles (solid blue and purple lines), higher than the results in the other cases. Fig. 2b shows the voltage profiles in the 1st and 10th cycles in the different electrolytes. The cathodic and anodic voltages were symmetrically below and above 0 V. Compared to the Li electrolyte (dashed red lines), the overpotentials in the Li–Ca and Li–Ba electrolytes were significantly increased in both the deposition and dissolution processes (dotted orange and green lines), suggesting the occurrence of surface passivation. Conversely, the overpotentials in the Li–La and Li–Ce electrolytes were close to those in the Li electrolyte, while the dissolution capacities were markedly increased. In addition, the voltage curve of the 10th deposition showed an increase in overpotential around the areal capacity of 1.5–2.0 mA h cm^{-2}, which was not observed in the 1st deposition. This difference would strongly depend on the surface conditions. In the first cycle, the deposition occurred on a bare Cu foil, where the deposits would grow from the electrode surface to the electrolyte under relatively uniform electric and diffusion fields. As the deposits cannot be completely dissolved, subsequent depositions must take place under much more complicated surface conditions. Although further investigation is necessary, we think that the inactive deposits remaining on the electrodes contain areas where lithium is preferentially deposited. Once these areas are filled, additional driving forces are required to continue the Li deposition, which would cause an increase of overpotential as observed in the 10th deposition.

To compare the deposition morphology, we conducted Li deposition/dissolution using three-electrode batch cells. In the batch cells, the Cu foil WE and the Li foil CE were separated in 5 mm without a separator. The absence of a separator allowed

us to study the morphology changes independently of the external stress. Fig. S1b† shows the structure of the batch cells. Li foil RE was inserted into the electrolyte between WE (Cu foil) and CE (Li foil). The Li deposition and dissolution were initially performed for 9 cycles and stopped after the 10th deposition. The current density was 1 mA cm^{-2} and the deposition capacity was fixed to 2 mA h cm^{-2}. The corresponding electrochemical results are shown in Fig. S2.† The photos of the Cu foil WEs after the 10th Li deposition are shown in the upper in Fig. 2c. The deposits in the Li–Ca and Li–Ba electrolytes were more uneven than those in the Li electrolyte, whereas the deposits in the Li–La and Li–Ce electrolytes exhibited more flat morphology. In addition, the electrolytes in the batch cells were extracted into glass beakers after the experiments, as shown in the lower in Fig. 2c. The grey deposits floating in the electrolytes would be fine inactive Li deposits peeling off from the Cu foil electrodes, which is known as "dead Li".[25] Impressively, the Li–La and Li–Ce electrolytes were kept transparent compared to the other electrolytes, suggesting an effective suppression of "dead Li". Based on the cycle test results in Cu||Li half cells, we demonstrated that the lanthanide salts have superior effectiveness as electrolyte additives in $[TFSI]^-$/EC–PC electrolytes to flatten the deposition morphology, reduce the formation of "dead Li", and consequently improve the coulombic efficiency of repeated Li deposition and dissolution.

Morphology changes during cycling

To understand the effects of the multivalent salt additives on the Li deposition/dissolution behaviour, we compared the morphology changes in the initial cycles in Cu||Li batch cells. For the electrolytes, the Li, Li–Ca and Li–La electrolytes were focused as representative. Fig. 3a–c shows the SEM images of the electrodeposits on Cu foil WEs after the 1st deposition, the subsequent 1st dissolution and the 2nd deposition in the Li, Li–Ca and Li–La electrolytes, respectively. The enlarged views are shown in Fig. S3–S5.† As shown in Fig. 3a, the deposits in the Li electrolyte after the 1st deposition showed a hilly landscape. In the cross-section view, a relatively dark and flat area was formed close to the Cu foil and a light and hilly area was formed above the dark area. The contrast between the light and dark areas would be related to the proportion of the SEI compositions in the deposits. The SEI compositions (C, N, O, S, F) contain more electrons than Li, resulting in higher secondary electron emission and a lighter appearance. In general, at the beginning of Li deposition, the Li^+ concentration on the electrode is high and homogeneous, and the Li deposits undergo an epitaxial growth behaviour into a dense and flat morphology. As the Li deposition progresses, the Li^+ concentration decreases and fluctuates, and the Li deposits change to a porous and uneven morphology.[3,26] During the subsequent 1st dissolution, the dark area almost disappeared, while the light hilly area was remained, containing the SEI components and the inactive Li particles that lost the electrical connection to the electrode. In the 2nd deposition, the dark areas (mainly Li metal) were reformed close to the Cu foil and mixed within the light areas (mainly SEI composition). Besides, cracks were observed in the deposits, which would make it easier for the deposits to peel away and float into the electrolytes, as observed in Fig. 2c.

In contrast, as shown in Fig. 3b and c, the deposits in the Li–Ca and Li–La electrolytes have a flatter surface compared to the deposits in the Li electrolyte. The change in surface morphology confirmed that the multivalent cation additives can alleviate the fluctuation in concentration distribution and electric field on the electrode.[16,27] On the cross section of the deposits in the Li–Ca electrolyte, the Li metal (dark areas) and the SEI compositions (light areas) were finely mixed in the deposits after the 1st deposition, and a similar structure was maintained in the subsequent dissolution and deposition. The Li metal mixed in the SEI compositions away from the Cu foil current collector would easily lose the electrical connection, causing the capacity loss in Fig. 2a. On the other hand, the deposits in the Li–La electrolyte showed a flat layered structure during the repeated Li deposition and dissolution. The Li metal layer (dark area) was formed reversibly on the Cu foil current collector and was not mixed into the surface SEI layer (light area), which would contribute to the higher coulombic efficiency in Fig. 2a. The difference between the Li, Li–Ca and Li–La cases was also confirmed after the 3rd deposition (see Fig. S6†).

The different pattern of the dark and light areas would be attributed to the stability and functionality of the SEI. Fig. 3d–f shows the chemical compositions on the surface of the deposits in the Li, Li–Ca, Li–La electrolytes, measured by energy-dispersive X-ray (EDX) spectroscopy. As Li cannot be detected by EDX, it was excluded from the results. The C, N, O, F, S came from the cathodic decomposition of the electrolyte species and formed SEI with the cations. For the deposits in the Li electrolyte, O had the highest atomic concentration, indicating that mainly EC and PC solvents contributed to the SEI formation. Besides, the surface composition was highly variable with repeated deposition and dissolution, indicating the insufficient stability of the SEI. On the other hand, the F concentration was significantly increased in the Li–Ca and Li–La electrolytes. Since F, S and N were contained by $[TFSI]^-$, such a composition change confirmed that $[TFSI]^-$ was promoted to participate in the SEI formation. In addition, the composition ratio was remarkably stable during deposition and dissolution in the Li–La electrolyte. The participation of La^{3+} would be more suitable than Ca^{2+} to improve the stability and functionality of the SEI in dilute $[TFSI]^-$/EC–PC electrolytes, which was also confirmed by the electrochemical impedance spectroscopy (EIS) measurements (see Fig. S7†).

Solid-electrolyte interphase formation

To investigate the chemical state of the SEI compositions, we conducted X-ray photoelectron spectroscopy (XPS) on the SEI formed on the Cu foils in different electrolytes. The Cu foils were first kept at 0 V for 6 hours to form SEI in Cu||Li coin cells. As there were no obvious deposits formed on the electrodes, the influence of the deposition morphology on the XPS spectra was ignored. Fig. 4a compares the Li 1s, O 1s, F 1s and La 3d spectra. In addition to the Li electrolyte (0.5 M) and the Li–La electrolyte, 0.8 M Li[TFSI] in EC–PC and 0.1 M $La[TFSI]_3$ in EC–PC (the La

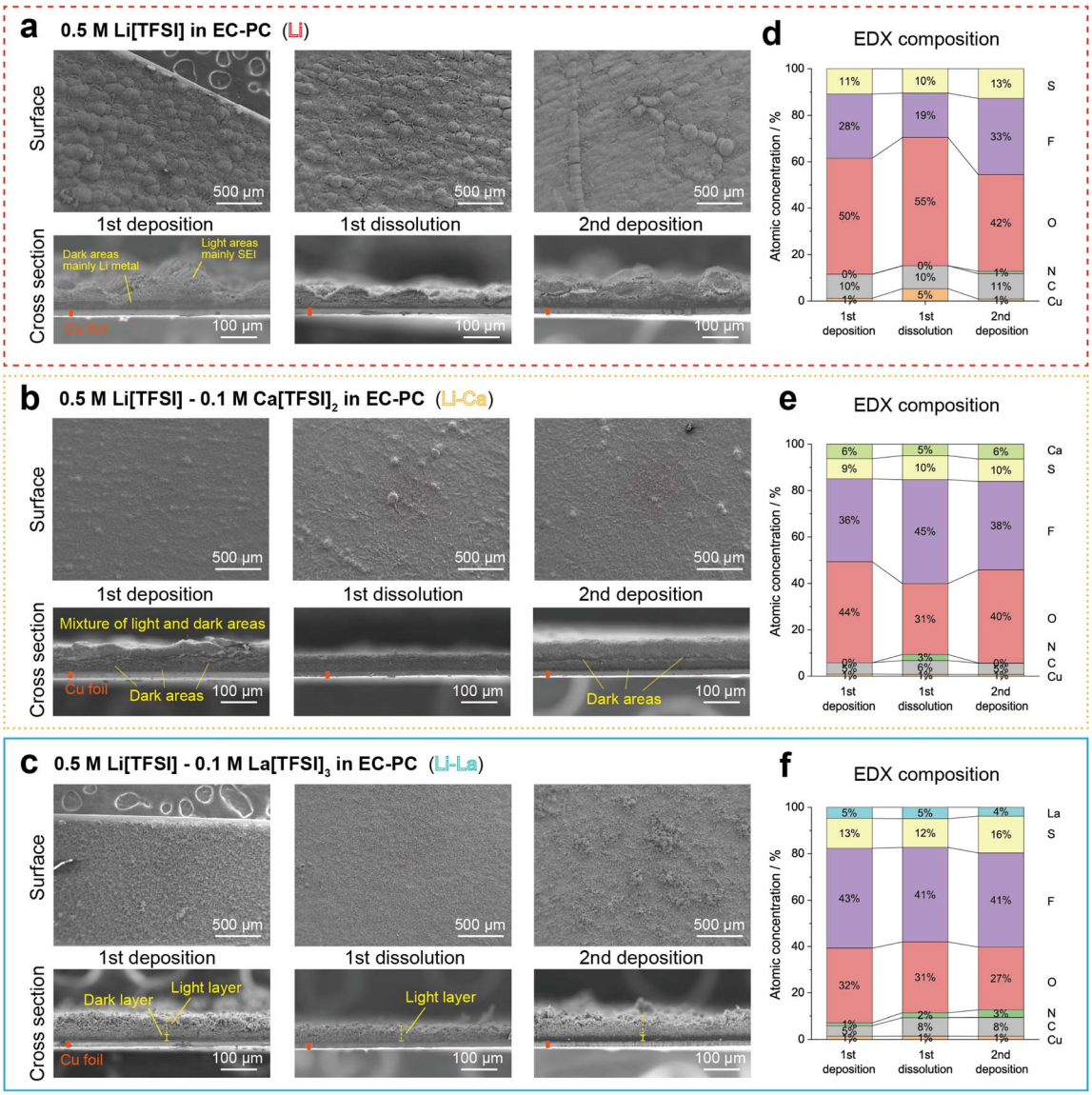

Fig. 3 Morphology changes and surface composition of electrodeposits during Li deposition/dissolution in Cu||Li batch cells with different electrolytes. (a–c) SEM images of front side and cross section views of electrodeposits on Cu foil current collectors after the 1st deposition, the 1st dissolution, and the 2nd deposition in (a) the Li electrolyte, (b) the Li–Ca electrolyte and (c) the Li–La electrolyte. Enlarged views are given in Fig. S3–S5.† The multivalent cation additives effectively flattened the deposition morphology. Besides, the La^{3+} additives enabled the reversible formation of a flat and dense Li metal layer during repeated Li deposition and dissolution, which would result in the high coulombic efficiency in Fig. 2a. (d–f) Surface composition of electrodeposits measured by energy dispersive X-ray (EDX) spectroscopy after the 1st deposition, the 1st dissolution and the 2nd deposition in (d) the Li electrolyte, (e) the Li–Ca electrolyte and (f) the Li–La electrolyte. The C, N, O, F, S came from the cathodic decomposition of $[TFSI]^-$ and EC, PC and formed SEI with the cations. The La^{3+} additive significantly improved the chemical stability and functionality of the SEI.

electrolyte) were also used for comparison. The binding energies of typical SEI compositions were shown with reference to previous works.[28–30] For Li[TFSI] in EC–PC, the peak positions did not changed significantly between 0.5 M and 0.8 M (red and dark red curves). Besides, the intensity of O 1s and F 1s was increased, suggesting that the SEI became denser with increasing salt concentration. However, the cycle tests in Cu||Li half cells confirmed that the coulombic efficiency was not obviously improved in 0.8 M Li[TFSI] in EC–PC (see Fig. S8†). This suggests that the composition rather than the amount of SEI plays an important role. In contrast, for SEI formed in the Li–La electrolyte (light blue curve), the binding energies of Li 1s and F 1s were decreased. In particular, the peak centre of F 1s was close to the result in the La electrolyte (blue curve), suggesting that F was essentially bound to La rather than Li. In addition, the O 1s peaks in the Li–La electrolyte became broader compared to the results in the Li electrolyte. The Li–O and La–O or Li–La–O compounds would be mixed in the SEI formation. The involvement of La compositions in the SEI would help to improve the structural stability while maintaining the electronic shielding and Li ionic conduction.

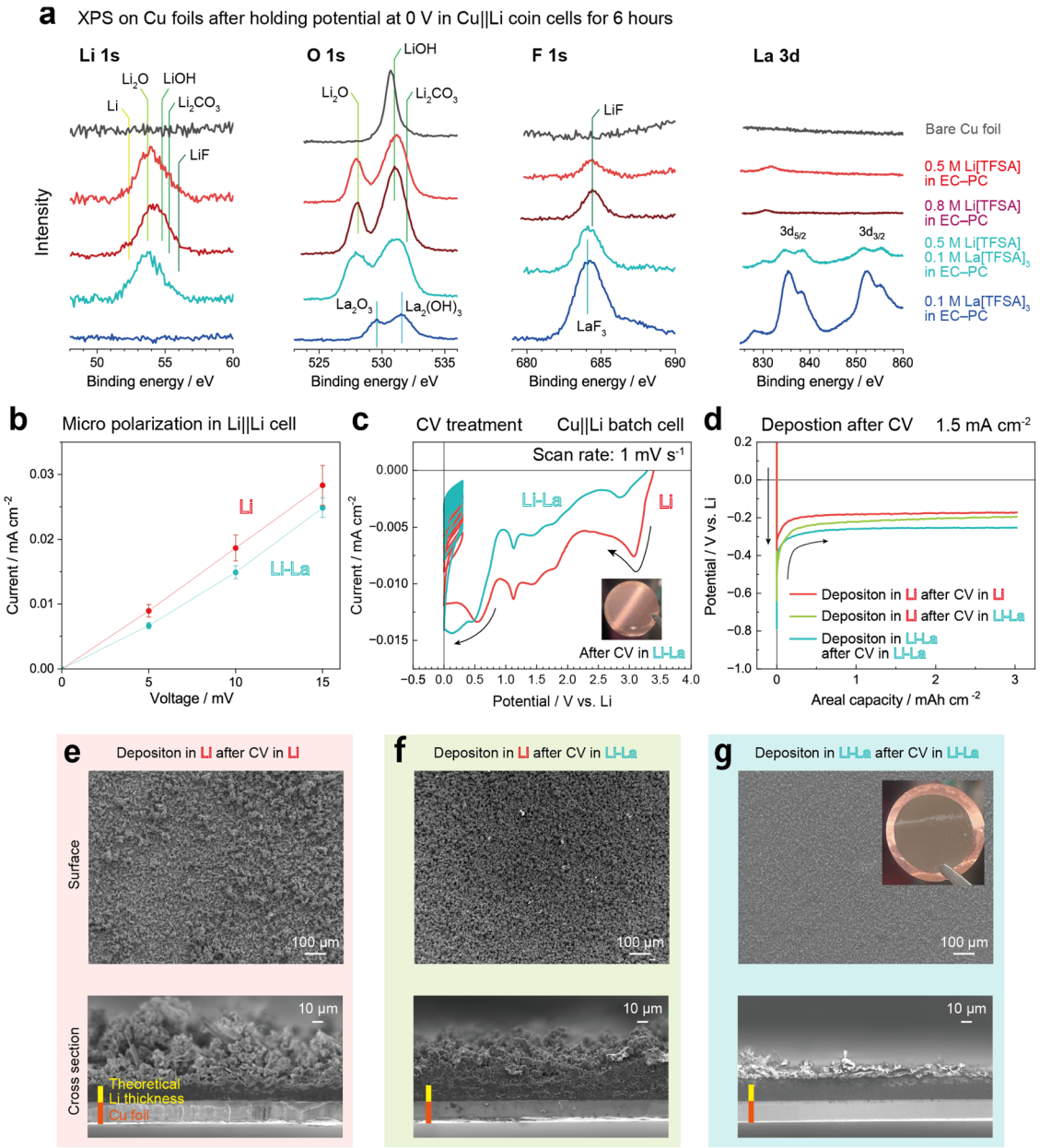

Fig. 4 Chemical state and structural stability of solid electrolyte interphase (SEI). (a) X-ray photoelectron spectroscopy (XPS) profiles of SEI formed on Cu foils by keeping the electrode potential at 0 V in Cu||Li coin cells with different electrolytes. For Li[TFSI] in EC–PC, increasing the salt concentration from 0.5 M to 0.8 M did not markedly change the XPS profiles. In contrast, adding La[TFSI]$_3$ changed the chemical state of Li, O, F in SEI, which would contribute to maintain a reversible Li deposition/dissolution. (b) Current density under micro polarization conditions (5, 10 and 15 mV) in Li||Li symmetric cells with the Li and Li–La electrolytes. The La salt additives suppressed the fluctuations between samples and slightly decreased current density (reaction kinetics) of interfacial reaction processes. (c) Current density profiles in cyclic voltammetry (CV) treatment to prepare sufficient SEI on Cu foil anodes in Cu||Li batch cells with the Li and Li–La electrolytes. The electrode potentials were scanned from the open circuit potentials (OCP) to 0 V *vs.* Li and then scanned in 0.3–0 V for 20 cycles. The cathodic current was decreased around 3–1 V and was increased around 0.5–0 V in the Li–La electrolyte, suggesting that adding La[TFSI]$_3$ modified the electrolyte species and affected their decomposition behaviour. The inset shows the photo of the Cu foil electrode after CV treatment in the Li–La electrolyte. No obvious deposits were observed. (d) Potential profiles in constant current deposition after CV treatment in Cu||Li batch cells with different electrolyte combinations. The La [TFSI]$_3$ additive moderated the rapid interfacial reaction and increased the overpotential during Li deposition. (e–g) SEM images of electrodeposits after constant current deposition. The CV treatment in the Li–La electrolyte improved the uniformity of the deposits in the Li electrolyte. More impressively, the Li deposits in the Li–La electrolyte exhibited a superior flat and dense morphology close to the ideal condition. The inset in (g) shows the photo of the Cu foil after deposition.

To investigate changes in the reaction kinetics of interfacial processes on Li metal anodes, we measured the current density under micro-polarisation conditions (5, 10, 15 mV) in Li||Li symmetric cells with the Li and Li–La electrolytes. More than three samples were used for each condition. Fig. 4b shows the current density at different polarization voltages. The current

densities in the Li–La electrolyte were lower than in the Li electrolyte at all applied voltages. Besides, the variation between the samples (error bars) in the Li–La electrolyte was narrower. Since the voltage and current density were very low, the kinetics of ion transport in the electrolyte and the morphology change can be basically ignored. Therefore, the decrease in the current density in the Li–La electrolyte would be attributed to an increase in the activation energy of the interfacial processes, including the (de)solvation of Li^+ with the coordinated solvent and anions, and also the ionic conduction through the SEI. Therefore, the decrease in the current density would result from the change of solvation structure,[16] and also from the more stable electrode–electrolyte interface formed on the Li metal.

To clearly compare the SEI functionality in different electrolytes during Li deposition, we conducted cyclic voltammetry (CV) treatment on Cu foils and then conducted constant current electrodeposition in Cu||Li batch cells. In the CV treatment, the potential was scanned from open circuit potential (OCP) to 0 V *vs.* Li and then cycled in the potential range of 0–0.3 V for 20 times, where SEI would sufficiently form on Cu foils. Fig. 4c shows the CV profiles in the Li and Li–La electrolytes. From OCP to 0 V, the current density was gradually increased with the appearance of several cathodic current peaks. As shown in the inset in Fig. 4c, there were no visible decomposition products on the Cu foil after CV treatment. Compared to the Li electrolyte, the current density decreased in the potential range above 1 V and increased significantly between 0 and 1 V in the Li–La electrolyte. This would be related to the promotion of anion decomposition instead of solvent and corresponded to the change in the SEI composition as observed in Fig. 3d–f and 4a. In the cyclic potential scan in the range of 0–0.3 V, the cathodic current gradually decreased near 0, indicating that the SEI formation basically shielded the electronic conduction between the Cu foil and the electrolyte. After CV treatment, the Cu foils were washed with EC–PC solvent and then assembled into clean batch cells for constant current deposition. For the Cu foil prepared in the Li electrolyte, the subsequent deposition was also conducted in the Li electrolyte. On the other hand, for the Cu foils prepared in the Li–La electrolyte, subsequent deposition was conducted in both the Li and Li–La electrolytes (green and blue curves, respectively) to determine whether La^{3+} must be continuously present in the electrolyte.

Fig. 4d shows the potential profiles in the deposition experiments. The electrodeposition after CV treatment in the Li–La electrolyte showed the highest overpotential (light blue curve). The electrodeposition in the Li electrolyte after CV in the Li–La electrolyte (green curve) showed the second highest overpotential, and the electrodeposition after CV in the Li electrolyte (red curve) showed the lowest overpotential. The SEI formed in the Li–La electrolyte would regulate the Li deposition process with less exposure of fresh surface and less increase in surface area. This reduces the exchange current density and results in a higher overpotential to drive the electrodeposition, consistent with the micro polarization measurement results in Fig. 4b. Fig. 4e–g compares the SEM images of the deposits formed in the different electrolyte combinations. For the deposits formed in the Li electrolyte (Fig. 4e and f), the hilly landscape was remarkably suppressed compared to the deposits obtained without CV treatment (Fig. 3a). The CV treatment in the Li–La electrolyte further improves the formation of a uniform and dense morphology. However, the mossy Li deposits were still formed, which could be attributed to the gradual degradation (cracking) of the SEI during deposition. In contrast, the electrodeposition in the Li–La electrolyte after CV treatment in the Li–La electrolyte showed an impressive flat and dense morphology (Fig. 4g). The thickness of the deposits was very close to the theoretical Li thickness of about 15 μm for an areal capacity of 3 mA h cm^{-2}. The results indicated that both the La composition in the electrolyte and in the SEI played a significant role in improving the Li deposition morphology.

Solvation environment modification

Since the SEI formation is related to the solvation structure in electrolytes, we conducted experimental Raman spectroscopy and computer simulations on the different electrolytes. Fig. 5a compares the Raman spectra of the Li, La and Li–La electrolytes. The solvents (PC, EC–PC) were also measured for comparison. In the Raman spectra, the peak around 900 cm^{-1} was the vibration of EC molecules,[31] where bound EC had a higher wavenumber than free EC and can be identified as shoulder peaks. The peak centres of bound EC were found to be different for Li^+ and La^{3+}. In the concentration range of 0.1–0.5 M, the peak centres of the bound EC were not obviously moved in the electrolytes with Li^+ or La^{3+} alone (see Fig. S9†). This feature indicates that the solvation structure was not markedly changed in the single cation cases in the dilute electrolytes. In contrast, as shown in Fig. 5b, peak fitting indicated that the peak centres of the bound EC moved to high wavenumbers for both Li^+ and La^{3+} in the Li–La electrolyte. Besides, the intensity ratio of EC coordinated to Li^+ was increased, and the intensity ratio of EC coordinated to La^{3+} was decreased in the Li–La electrolyte as shown in Fig. 5c. These changes in peak centres and intensity ratios of the bound EC suggest that the solvation structures of the cations were altered in the Li–La electrolyte. In addition, the vibration mode of PC (around 850 cm^{-1}) and $[TFSI]^-$ (around 740 cm^{-1}) was not obviously changed in the dilute electrolytes, which cannot provide further evidence to determine the solvation structure.

To estimate the coordination number of the anions and solvent molecules to the cations, molecular dynamics (MD) simulations were performed on the Li, La and Li–La electrolytes. For the force parameters, the general AMBER force field (GAFF2)[32] was used for Li^+, $[TFSI]^-$ ions and EC, PC, and the universal force field (UFF)[33] was used for La^{3+}. Details are given in the Experimental section. Since $[TFSI]^-$ and EC, PC are basically coordinated to cations by O, the partial distribution functions between cation and O were computed by MD and converted to the coordination numbers. Fig. 5d and e shows the coordination numbers of the solvent molecules and $[TFSI]^-$ anions, respectively. The corresponding radial distribution function plots are shown in Fig. S10.† For EC and PC coordinated to Li^+, the bound EC increased, and the bound PC decreased in the Li–La electrolyte model compared to the Li

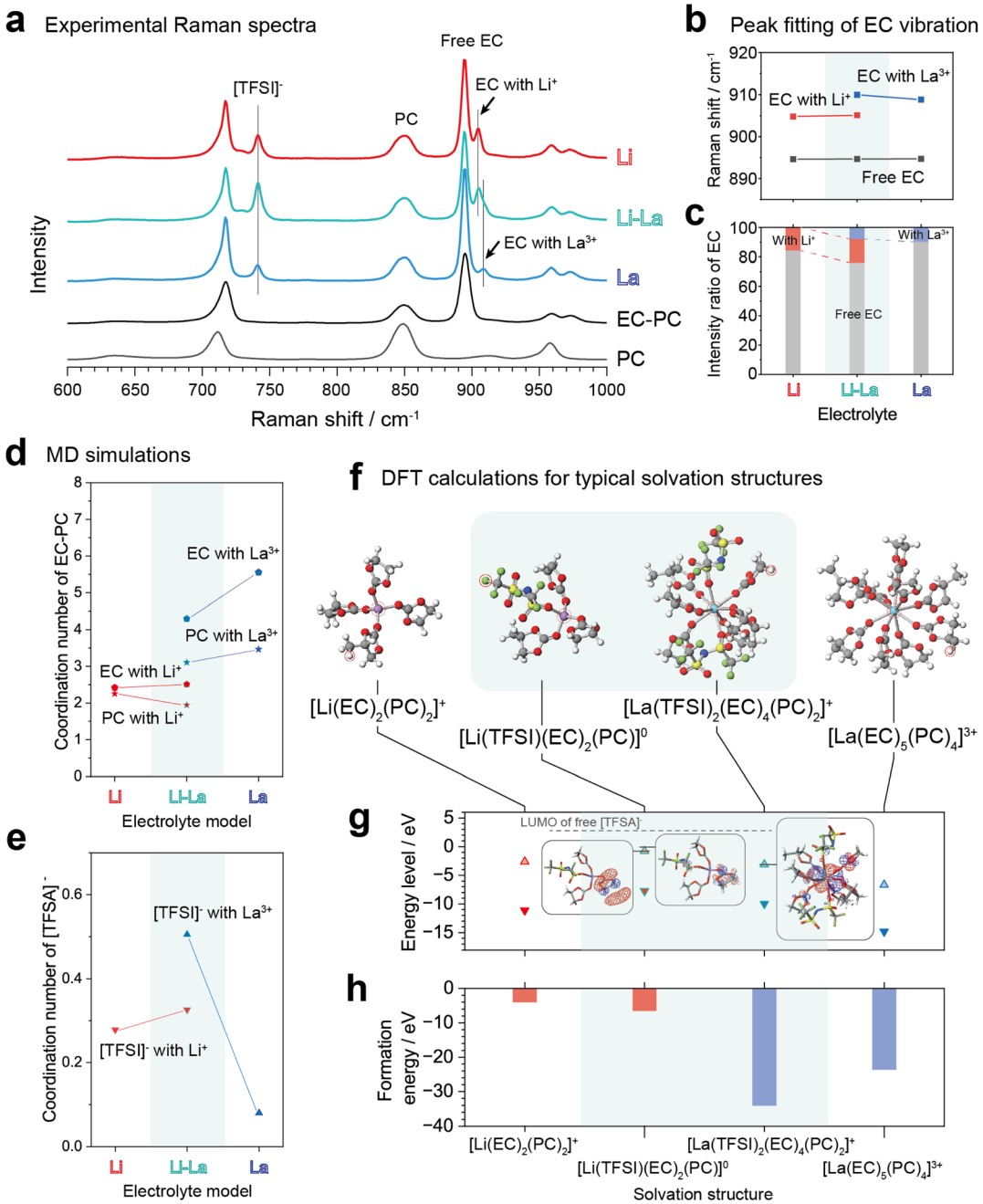

Fig. 5 Raman spectra and computer simulations on solvation structure in the Li and Li–La electrolytes. (a) Raman spectra in the wavenumber range of 600 cm^{-1} to 1000 cm^{-1}. The peak at about 740 cm^{-1} corresponds to the expansion and contraction vibration mode of $[TFSI]^-$. (b) Peak centres and (c) intensity ratio of free and bound EC. The intensity ratio changes indicated the changes in coordination numbers. (d–e) Coordination numbers of (d) EC, PC and (e) $[TFSI]^-$ to Li^+ and La^{3+} obtained in the MD simulations. The corresponding radial distribution function plots are shown in Fig. S10.† The coordination number of the solvent molecules was decreased and the coordination number of $[TFSI]^-$ was increased for both cations in the Li–La electrolyte. The computational results of the coordination numbers were agreed with the experimental Raman spectra. (f) Typical solvation structures in the different electrolytes based on the MD simulation results. The solvation structures were optimized by first-principles calculations using Gaussian 16. Note each O in $[TFSI]^-$ coordinating to a cation was counted as the coordination number of 0.25 in the MD results. (g) HOMO and LUMO levels and (h) formation energy of the solvation structures. Insets in (g) show the molecular orbitals with respect to the energy levels indicated by horizontal bars. The CIP-state $[TFSI]^-$ has a lower LUMO level compared to the free state and is therefore promoted to decompose in the SEI formation.

electrolyte model. On the other hand, both the EC and PC bound to La^{3+} decreased in the Li–La electrolyte compared to the La electrolyte model. The changes in the coordination numbers of EC were in consistent with the changes in the intensity ratio of the EC peaks in the Raman spectra (Fig. 5c). On the other hand, the coordination numbers of $[TFSI]^-$ were

increased for both Li^+ and La^{3+} in the Li–La electrolyte model compared to the single cation cases. This trend was consistent with the chemical shift of ^7Li measured by the nuclear magnetic resonance (NMR) spectroscopy (see Fig. S11†). The ^7Li chemical shift moved to the negative side in the Li–La electrolyte compared to the Li electrolyte, suggesting an increase in electron density around Li^+, which would come from the directly coordinated anions (CIPs). The CIP formation promoted in the dual-cation electrolytes would be driven by Coulomb interactions between cations of different valence states to reduce the free energy of the electrolyte system.[16]

The change in solvation structure would affect the energy levels of the molecular orbitals associated with the electrolyte decomposition to form the SEI. Therefore, we conducted density functional theory (DFT) calculations by Gaussian 16,[34] to estimate the binding energies, and the HOMO and LUMO energy levels of the typical solvation structures based on the experimental Raman spectra and the MD results. The DFT calculations were performed using the B3LYP hybrid functional,[35] with the 6-311++g** basis set,[36] for Li^+, $[TFSI]^-$, EC and PC, and lanl2dz basis set,[37] for La^{3+}. Fig. 5f shows four representative complexes after structural optimization. Fig. 5g shows the HOMO and LUMO levels of each complex and Fig. 5h shows the formation energies. Compared to the SSIP-state $[Li(EC)_2(PC)_2]^+$ and $[La(EC)_5(PC)_4]^{3+}$, the CIP-state $[Li(TFSA)(EC)_2(PC)]^0$ and $[La(TFSA)_2(EC)_4(PC)_2]^+$ had lower formation energies and higher HOMO and LUMO levels. During Li deposition, the strongly bound CIP-state Li^+ would require a higher activation energy for desolvation,[38] which helps to retard the cation depletion on the electrode surface and to maintain a uniform morphology. In addition, the solvated EC and PC in CIPs had higher LUMO levels than those in SSIPs, which would moderate the cathodic decomposition of EC and PC. On the other hand, $[TFSI]^-$ in CIPs has a much lower LUMO level compared to the free $[TFSI]^-$ (dashed grey line in Fig. 5g), which would result in the promoted cathodic decomposition of $[TFSI]^-$. As a result, the solvent-derived SEI formation changed to anion-derived SEI formation as the ratio of CIPs increased. In addition, although the significantly low binding energy of the La^{3+}-complexes is considered to prevent the reduction of La^{3+}, the cathodic decomposition of the complexes would be involved in the SEI formation. Thus, it can be concluded that, from the above two factors (*i.e.*, the CIP formation of Li ion and anion-derived SEI involving La^{3+} ions), the addition of the lanthanide salts contributed to a uniform deposition morphology and stable SEI formation on Li metal anodes.

Full-cell tests with $LiFePO_4$ cathodes

To test the effectiveness of the lanthanide salt additives in full cells, we assembled $LiFePO_4$||Cu coin cells with the Li and Li–La electrolytes. Since no excess Li is used, such cells are usually referred to as "anode-free" cells. Fig. 6a shows the capacity retention and coulombic efficiency over 20 cycles. The Li–La electrolyte (light blue markers and lines) markedly improved the cyclability compared to the Li electrolyte (red markers and lines). Fig. 6b shows the voltage profiles in cycle 1 and 20. In cycle 1, the charge curves in the Li and the Li–La electrolytes were similar. However, the discharge curve in the Li–La electrolyte dropped to the cutoff voltage (3 V) earlier than in the Li electrolyte. The larger irreversible capacity could be caused by the involvement of La^{3+} complexes in the SEI formation in the Li–La electrolyte. The optimization of salt concentration (see Fig. S12†), anion and solvent combination and the charging/discharging protocols will be important strategies to minimize this irreversible capacity. Although the initial capacity loss was slightly higher, the capacity retained in the Li–La electrolyte at cycle 20 was approximately twice that of the Li electrolyte. In addition, the overpotential increase in the Li–La electrolyte was significantly less than that in the Li electrolyte, and also observed in the Li||Li symmetric cells (Fig. S13†). Since the redox reactions of $FePO_4/LiFePO_4$ and Li^+/Li have basically constant equilibrium potentials, the overpotential increase would be related to the internal resistance in the cells.

Fig. 6c and d show the electrochemical impedance spectroscopy (EIS) profiles during cycling in the Li and Li–La electrolytes, respectively. The semicircular part in the high frequency range (10 kHz–10 Hz) corresponds to the electron and ion transfer at the electrode–electrolyte interface, and the uphill part in the low frequency range (1 Hz–10 mHz) is related to the solid-state diffusion and phase transformation in the intercalation-type cathodes. During cycling, the semicircular part became larger in the Li electrolyte. In contrast, the semicircular part was flatter and almost unchanged during cycling in the Li–La electrolyte, indicating a superior interfacial stability. Moreover, the uphill part was higher in the Li–La electrolyte than in the Li electrolyte, suggesting that the La^{3+} may have some influence on the reaction kinetics of Li^+ intercalation into $LiFePO_4$. Fig. 6e shows the cation ratio in $LiFePO_4$ cathodes measured by ICP after 1st charge and 1st discharge in a $LiFePO_4$||Li coin cell with the Li–La electrolyte. As no obvious amount of La was detected, the Li (de)intercalation was confirmed to be the dominant cathode reaction. In addition, the coin cells were disassembled after 20 cycles and the deposits remaining on the Cu foil anodes were analysed. The amount of metallic Li^0, which was isolated during cycling, was detected from the amount of H_2 produced by the reaction with pure water. The remaining deposits (almost electrolyte decomposition products) were then measured for Li composition by ICP analysis. Fig. 6f compares the masses of Li^0 and Li^+ composition in the deposits obtained in the Li and Li–La electrolytes. Both the masses of Li^0 and Li^+ were decreased in the Li–La electrolyte compared to the Li electrolyte, confirming that the La salt additive effectively improved the SEI functionality to decrease the loss of carrier ions (Li^+) during cycling. However, it should be noted that the La salt additive would increase the capacity loss for the SEI formation in early cycles. Therefore, using an excessive amount of Li on the anodes can more clearly demonstrate the effectiveness, although it is impractical due to increased production costs and reduced energy density.

Fig. 6g and h shows the cycle tests in $LiFePO_4$||Li cells with the Li and Li–La electrolytes. For the Li electrolyte, due to the lack of a stable electrode/electrolyte interface, the internal resistance was significantly increased during cycling and the

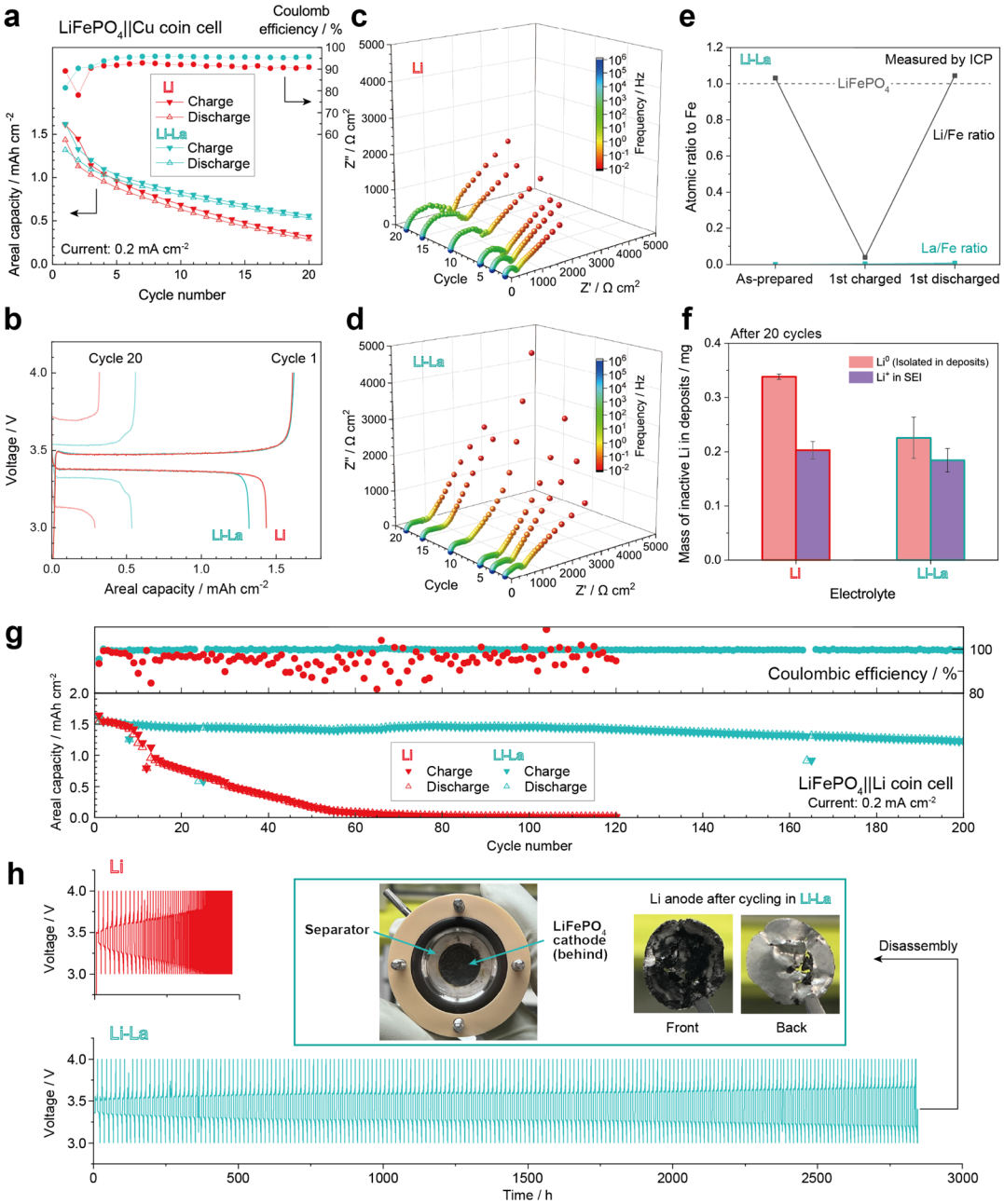

Fig. 6 Full cell tests with $LiFePO_4$ cathodes. (a) Capacity retention and coulombic efficiency of $LiFePO_4$||Cu coin cells with the Li and Li–La electrolytes. (b) Voltage profiles in cycle 1 and 20 in $LiFePO_4$||Cu cells. The La salt additives markedly improved the cyclability and moderated the overpotential increase during cycling. (c and d) Electrochemical impedance spectroscopy (EIS) profiles of $LiFePO_4$||Cu cells with (c) the Li electrolyte and (d) the Li–La electrolyte. The La salt additive effectively prevented the resistance increase of the interfacial processes in the high frequency range during cycling. (e) Chemical composition changes of $LiFePO_4$ charged and discharged in the Li–La electrolyte. The La salt additive had no apparent effect on Li (de)intercalation. (f) Mass of inactive Li composition in the deposits after 20 cycles in the $LiFePO_4$||Cu cells with different electrolytes. The stable SEI layer formed in the Li–La electrolyte significantly decreased the inactive Li metal particles isolated in the deposits and suppressed the consumption of Li^+ ions in the SEI formation. (g) Capacity retention and (h) voltage profiles of $LiFePO_4$||Li cells with the Li and Li–La electrolytes. The excess Li (200 μm thickness) on the anode significantly improved the cyclability in the Li–La electrolyte. In contrast, the rapid increase in internal resistance resulted in poor cyclability in the Li electrolyte even with excess Li. The $LiFePO_4$||Li cell with the Li–La electrolyte was disassembled after 200 cycles and the photos of the electrodes are shown in the inset. The Li foil anode basically remained as a bulk without significant pulverisation. The cracks in the centre of the Li foil anode occurred when peeling it off from the separator.

reversible capacity went to 0 very quickly even with an excess amount of Li (200 μm thickness). The capacity-fade relaxation cycle (n_0) was estimated to be about 26 cycles after fitting $\exp(-n/n_0)$, see Fig. S13.† In contrast, for the Li–La electrolyte, the excess Li compensated for the irreversible capacity loss in the SEI formation in the early cycles, further brought

highlighting the effects of the La salt additives. The cyclability was significantly improved in the Li–La electrolyte and no significant capacity degradation was observed up to 200 cycles; n_0 was estimated to be about 1000 cycles. In addition, as shown in the inset of Fig. 6h, the Li foil anode was basically maintained as a bulk structure without pulverization, suggesting that the thickness of the Li foil anode can be decreased to a more practical value to increase the energy density. The effectiveness of the La[TFSI]$_3$ additive was also demonstrated in $LiFePO_4$||Cu cells with commercial 1 M $LiPF_6$/EC–DMC electrolyte (Fig. S14†), which confirmed the versality of this strategy. In addition, the cycle tests with the present coin cells (Fig. S1a†) had a low pressure on the electrodes, which makes it easy to evaluate the effects of the multivalent additives, but may lead to an underestimation of the cyclability.[39] For example, a 2032-type cell can show better cyclability (Fig. S15†) and rate capability (Fig. S16†), which would be preferred in evaluating the battery performance in future.

Conclusions

By comparing the effects of different multivalent salts (Ca[TFSI]$_2$, Ba[TFSI]$_2$, La[TFSI]$_3$, Ce[TFSI]$_3$) as electrolyte additives, we have shown that the lanthanide salts can effectively improve the coulombic efficiency of Li metal anodes in carbonate-based electrolytes (Li[TFSI]/EC–PC). As shown in the present case, La^{3+} ion is hard to be inserted into the cathode materials generally, so we can regard such multivalent cation as additives to modify the solvation structure and stabilizer of the SEI for Li-metal battery systems. The mixing of multivalent cations with monovalent cations promotes the close coordination of anions (CIPs) to mitigate the strong Coulomb interaction in the electrolyte systems. Anions in the CIP state have a lower LUMO level compared to the free state, which facilitates the cathodic decomposition of anions in the SEI formation. The involvement of anions, as well as the multivalent cations, significantly changes the composition ratio and chemical state of the SEI, with the lanthanide salts contributing to superior SEI stability and functionality in the carbonate-based electrolyte compared to the alkaline earth salts. Specifically, La–O and La–F in SEI would improve the structural strength and maintain the electron shielding and Li ionic conduction. Owing to these effects, the cyclability of Li metal anodes in Cu||Li half cells and "anode-free" $LiFePO_4$||Cu full cells was significantly improved. During Li deposition/dissolution, a flat and dense Li metal layer is reversibly formed on the Cu foil current collector and covered by a flat SEI layer containing the multivalent cations. The stable electrode structure prevents the internal resistance increase and retards the progressive electrolyte decomposition during cycling. In addition, it should be emphasized that, by using the CV treatment, the SEI layer can be reduced to very thin and the Li deposits are close to the ideal thickness in terms of the theoretical density.

To further improve the effectiveness of the multivalent cation additives, we need to understand how the Coulomb interaction works in different ion-solvent combinations and affects the solvation structure and SEI properties. Besides, expanding the candidate elements of cation additives (such as Mg^{2+}, Al^{3+}) is also important for advancing fundamental knowledge on the reaction behaviour and also from a cost perspective. The use of multivalent cations as electrolyte additives provides an approach to the development of electrolytes for advanced rechargeable Li batteries and other battery systems, where the concerted effects between the monovalent and multivalent cations shed a light on overcoming the fatal problems of the conventional metal-ion battery systems.

Experimental

Material preparation

Bis(trifluoromethanesulfonyl)imide, $[TFSI]^-$, salts (purity 99.5%) were purchased from SOLVIONIC Company and Kishida Chemical Co., Ltd. Ethylene carbonate, EC, and propylene carbonate, PC, solvents (purity >99.0%) were purchased from Kishida Chemical Co., Ltd. The electrolytes with different salt concentrations were prepared in gloveboxes (Miwa Mfg Co., Ltd and UNICO Ltd) filled with high purity argon atmosphere. For the electrodes, Cu foil current collectors (20 μm thickness) were purchased from Furuuchi Chemical Co., and lithium metal was purchased from Honjo Metal Co., Ltd. $LiFePO_4$ cathode sheets were purchased from Hohsen Corp. The areal capacity loading was approximately 1.5 mA h cm^{-2}.

Electrochemical measurements

Electrochemical experiments were conducted using a VMP-3 or VSP-300 potentiostat (Bio-Logic SAS). Constant current electrodeposition was conducted using two-electrode coin cells (SB2A, EC-frontier Co., Ltd) and three-electrode batch cells (SB1A, EC-frontier Co., Ltd). For the coin cell, the electrodes (circular 16 mm in diameter) were separated by a 20 μm-thick separator (#3501, Celgard LCC). For the batch cell, the working electrodes (WEs) and counter electrodes (CEs) were cut into circular 16 mm in diameter and has an effective area of 1.32 cm^2 (13 mm in diameter) contacting to electrolytes. Besides, pieces of Li foil were inserted between the WEs and CEs as the reference electrodes. Fig. S1† shows the construction of the batch cell and the coin cell. The cells were assembled and tested in gloveboxes filled with a high purity argon atmosphere.

Morphology observation

Electrodeposits were washed by dropping ethyl methyl carbonate, EMC, (99%, Merck KGaA) and then dried in an argon atmosphere. Photos of the electrodes were taken using a mobile phone (Sony Corporation or Apple Inc). Microstructures of the electrodeposits were observed in detail using a field emission scanning electron microscope (FE-SEM, JSM-7200F, JEOL Ltd). Samples were prepared in an argon atmosphere and transferred to the high vacuum chamber of FE-SEM without exposure to air. Cross section samples were prepared using a trimming cutter (CSC6, JEOL Ltd).

Chemical composition and valence state analyses

An energy dispersive X-ray spectroscopy (EDX) detector attached to the FE-SEM was used to measure the composition of the electrodeposits. X-ray photoelectron spectroscopy (XPS) was conducted using PHI5000 VersaProbe II (ULVAC-PHI, Inc). The samples were kept in an argon atmosphere with a transfer vessel. Inductively coupled plasma optical emission spectroscopy (ICP-OES) was entrusted to Analytical Research Core for Advanced Materials, Institute for Materials Research, Tohoku University. To estimate the inactive Li composition in the deposits after the full cell tests, the Cu foil anodes were first carefully washed by EMC and dried in an argon atmosphere. The electrodes were then immersed in distilled water to dissolve the isolated metallic Li, and the generated H_2 gas was collected and measured. The remaining undissolved deposits were then measured by ICP analysis to determine the amount of Li^+ involved in SEI.

Raman spectroscopy

Raman spectra of the electrolytes were measured at room temperature using a Raman spectrometer NRS-5100, JASCO Corporation. To allow the comparison of the intensity between different samples, each electrolyte was injected into a deep columnar container made of stainless steel, where the sample irradiated by the incident laser (532 nm) was fixed at a constant volume.

First-principles calculations

Density functional theory (DFT) calculations were conducted using the Gaussian 16 code,[34] with B3LYP hybrid functional,[35] and 6-311++G(d, p), lanl2dz basis set.[36,37] Raman activities of different complexes were estimated by normal frequency analyses. The formation energy of each complex was calculated according to $\Delta E = E(\text{complex}) - E(\text{cation}) - E(\text{anion}) - E(\text{EC}) - E(\text{PC})$, where E is the electronic energy of each species complemented with thermal free energy correction.

Molecular dynamics (MD) simulations

The MD simulations were performed with the LAMMPS code,[40] supported by a visualization software (Winmostar, X-Ability Co. Ltd). The solution models were constructed with 500 EC and 500 PC molecules as the solvent and the appropriate number of cations and $[TFSI]^-$ anions corresponding to the salt concentration. For example, the model of Li[TFSI]–La[TFSI]$_3$ in EC–PC consisted of 50 Li^+, 10 La^{3+} cations, 80 $[TFSI]^-$ anions, 500 EC and 500 PC. Each model was built in a cubic box with a random configuration of the species. The initial volume of each box was set according to the practical density of the corresponding electrolyte. The following procedures, based on previous studies,[41,42] were used to determine the force parameters to obtain valid simulation results. The cations were set to be fixed charge values and the pair interaction potentials were calculated based on the Lennard-Jones (LJ) potential with long-range Coulomb interaction (cut-off distance of 15 Å). The LJ parameters for Li^+ were adopted from the general AMBER force field (GAFF2)[32] and those for La^{3+} were adopted from unified force field (UFF).[33] For the $[TFSI]^-$, EC and PC, structure optimization was first conducted by DFT calculations (B3LYP/6-311++G(d, p) at Gaussian 16) and then the restrained electrostatic potential (RESP)[43] was calculated to determine the partial charges. The charge of each atom was fixed during the simulations. The force-field parameters (LJ, bond, angle, dihedral) were then generated using GAFF2. The Lorentz–Berthelot combining rules were employed to calculate the LJ potentials between cations with atoms in $[TFSI]^-$, EC and PC. The long-range forces (k-space) were computed using the particle–particle particle-mesh (PPPM).[44]

Data availability

The data supporting this article have been included as part of the ESI.†

Author contributions

T. I. supervised the research project. H. L. conceived the study. H. L. and D. S. designed the research plan. D. S. conducted the electrochemical experiments, morphology observation, composition analyses, Raman spectroscopy. H. L. conducted the XPS, first-principles calculations, molecular dynamics simulation and some supplementary electrochemical experiments. R. J. conducted some supplementary Raman spectroscopy. D. H., K. N., H. T., H. Y. and M. O. conducted the micro polarization analysis and measured the amount of inactive Li composition after full cell tests. H. L. wrote the manuscript. All authors discussed the results and contributed to this work.

Conflicts of interest

D. H., K. N., H. T., H. Y. and M. O. are employees of Toyota Motor Corporation. The other authors have no conflicts to declare.

Acknowledgements

The authors thank Analytical Research Core for Advanced Materials, Institute for Materials Research, Tohoku University for conducting the ICP analyses. The authors acknowledge Center for Computational Materials Science, Institute for Materials Research, Tohoku University for the use of supercomputer MASAMUNE-IMR (Project No. 2212SC0402). H. L. thanks Mariko Ando (Technical Division, School of Engineering, Tohoku University) for the NMR measurements. This research is partly being carried out as a joint research project between Tohoku University and Toyota Motor Corporation. This work is supported by Grant-in-Aid for Scientific Research (S) number 23H05452 and Grant-in-Aid for Early-Career Scientists number 24K17539 commissioned by Japan Society for the Promotion of Science (JSPS).

References

1 F. Duffner, N. Kronemeyer, J. Tübke, J. Leker, M. Winter and R. Schmuch, *Nat. Energy*, 2021, **6**, 123–134.
2 J. W. Xiang, L. Y. Yang, L. X. Yuan, K. Yuan, Y. Zhang, Y. Y. Huang, J. Lin, F. Pan and Y. H. Huang, *Joule*, 2019, **3**, 2334–2363.
3 P. Bai, J. Li, F. R. Brushett and M. Z. Bazant, *Energy Environ. Sci.*, 2016, **9**, 3221–3229.
4 K.-H. Chen, K. N. Wood, E. Kazyak, W. S. LePage, A. L. Davis, A. J. Sanchez and N. P. Dasgupta, *J. Mater. Chem. A*, 2017, **5**, 11671–11681.
5 X. Shen, R. Zhang, X. Chen, X. B. Cheng, X. Y. Li and Q. Zhang, *Adv. Energy Mater.*, 2020, **10**, 1903645.
6 F. Chu, J. Hu, J. Tian, X. Zhou, Z. Li and C. Li, *ACS Appl. Mater. Interfaces*, 2018, **10**, 12678–12689.
7 Q. Yang, J. Hu, J. Meng and C. Li, *Energy Environ. Sci.*, 2021, **14**, 3621–3631.
8 J. Meng, M. Lei, C. Lai, Q. Wu, Y. Liu and C. Li, *Angew. Chem., Int. Ed.*, 2021, **60**, 23256–23266.
9 Z. Li, W. Liang, J. Chen, L. Song, T. Xiong, W. Xie, S. Wu, D. Hu, X. Yao and Z. Peng, *Nano Energy*, 2023, **110**, 108370.
10 Z. Li, Z. Chen, N. Sun, D. Wang, X. Yao and Z. Peng, *Angew. Chem., Int. Ed.*, 2024, **63**, e202400876.
11 Y. He, L. Song, Z. Li, X. Yao and Z. Peng, *Nano Energy*, 2023, **118**, 109027.
12 L. Suo, Y.-S. Hu, H. Li, M. Armand and L. Chen, *Nat. Commun.*, 2013, **4**, 1481.
13 Y. Yamada, J. Wang, S. Ko, E. Watanabe and A. Yamada, *Nat. Energy*, 2019, **4**, 269–280.
14 D. M. Seo, S. Reininger, M. Kutcher, K. Redmond, W. B. Euler and B. L. Lucht, *J. Phys. Chem. C*, 2015, **119**, 14038–14046.
15 J. Qian, W. A. Henderson, W. Xu, P. Bhattacharya, M. Engelhard, O. Borodin and J. G. Zhang, *Nat. Commun.*, 2015, **6**, 6362.
16 H. Li, M. Murayama and T. Ichitsubo, *Cell Rep. Phys. Sci.*, 2022, **3**, 100907.
17 M. Wang, L. Huai, G. Hu, S. Yang, F. Ren, S. Wang, Z. Zhang, Z. Chen, Z. Peng, C. Shen and D. Wang, *J. Phys. Chem. C*, 2018, **122**, 9825–9834.
18 J. Moon, D. O. Kim, L. Bekaert, M. Song, J. Chung, D. Lee, A. Hubin and J. Lim, *Nat. Commun.*, 2022, **13**, 4538.
19 S. Chen, J. Zheng, D. Mei, K. S. Han, M. H. Engelhard, W. Zhao, W. Xu, J. Liu and J.-G. Zhang, *Adv. Mater.*, 2018, **30**, 1706102.
20 Y. Yu, C. Lai, M. Lei, K. Chen and C. Li, *Mater. Horiz.*, 2024, **11**, 2169–2179.
21 J. Forero-Saboya, C. Davoisne, R. Dedryvere, I. Yousef, P. Canepa and A. Ponrouch, *Energy Environ. Sci.*, 2020, **13**, 3423–3431.
22 S. Park, H. Liu, J. Quinn, S. H. Lapidus, Y. Zhang, S. E. Trask, C. Wang, B. Key and F. Dogan, *ACS Appl. Mater. Interfaces*, 2024, **16**, 20341–20351.
23 Y. Inaguma, C. Liquan, M. Itoh, T. Nakamura, T. Uchida, H. Ikuta and M. Wakihara, *Solid State Commun.*, 1993, **86**, 689–693.
24 S. Ohta, T. Kobayashi and T. Asaoka, *J. Power Sources*, 2011, **196**, 3342–3345.
25 K. Qin, K. Holguin, M. Mohammadiroudbari, J. Huang, E. Y. S. Kim, R. Hall and C. Luo, *Adv. Funct. Mater.*, 2021, **31**, 2009694.
26 A. Hagopian, M. L. Doublet and J. S. Filhol, *Energy Environ. Sci.*, 2020, **13**, 5186–5197.
27 F. Ding, W. Xu, G. L. Graff, J. Zhang, M. L. Sushko, X. Chen, Y. Shao, M. H. Engelhard, Z. Nie, J. Xiao, X. Liu, P. V. Sushko, J. Liu and J. G. Zhang, *J. Am. Chem. Soc.*, 2013, **135**, 4450–4456.
28 F. Ding, W. Xu, X. Chen, J. Zhang, M. H. Engelhard, Y. Zhang, B. R. Johnson, J. V. Crum, T. A. Blake, X. Liu and J.-G. Zhang, *J. Electrochem. Soc.*, 2013, **160**, A1894.
29 J. P. H. Li, X. Zhou, Y. Pang, L. Zhu, E. I. Vovk, L. Cong, A. P. van Bavel, S. Li and Y. Yang, *Phys. Chem. Chem. Phys.*, 2019, **21**, 22351–22358.
30 B. Zhao, J. Li, M. Guillaume, J. Dendooven and C. Detavernier, *J. Energy Chem.*, 2022, **66**, 295–305.
31 J. L. Allen, O. Borodin, D. M. Seo and W. A. Henderson, *J. Power Sources*, 2014, **267**, 821–830.
32 J. Wang, R. M. Wolf, J. W. Caldwell, P. A. Kollman and D. A. Case, *J. Comput. Chem.*, 2004, **25**, 1157–1174.
33 A. K. Rappe, C. J. Casewit, K. S. Colwell, W. A. I. Goddard and W. M. Skiff, *J. Am. Chem. Soc.*, 1992, **114**, 10024–10035.
34 M. J. Frisch, G. W. Trucks, H. B. Schlegel, G. E. Scuseria, M. A. Robb, J. R. Cheeseman, G. Scalmani, V. Barone, G. A. Petersson, H. Nakatsuji, X. Li, M. Caricato, A. V. Marenich, J. Bloino, B. G. Janesko, R. Gomperts, B. Mennucci, H. P. Hratchian, J. V. Ortiz, A. F. Izmaylov, J. L. Sonnenberg, D. Williams-Young, F. Ding, F. Lipparini, F. Egidi, J. Goings, B. Peng, A. Petrone, T. Henderson, D. Ranasinghe, V. G. Zakrzewski, J. Gao, N. Rega, G. Zheng, W. Liang, M. Hada, M. Ehara, K. Toyota, R. Fukuda, J. Hasegawa, M. Ishida, T. Nakajima, Y. Honda, O. Kitao, H. Nakai, T. Vreven, K. Throssell, J. A. Montgomery Jr, J. E. Peralta, F. Ogliaro, M. J. Bearpark, J. J. Heyd, E. N. Brothers, K. N. Kudin, V. N. Staroverov, T. A. Keith, R. Kobayashi, J. Normand, K. Raghavachari, A. P. Rendell, J. C. Burant, S. S. Iyengar, J. Tomasi, M. Cossi, J. M. Millam, M. Klene, C. Adamo, R. Cammi, J. W. Ochterski, R. L. Martin, K. Morokuma, O. Farkas, J. B. Foresman and D. J. Fox, *Gaussian 16*, Gaussian, Inc., Wallingford CT, 2016.
35 A. D. Becke, *J. Chem. Phys.*, 1993, **98**, 5648–5652.
36 R. Krishnan, J. S. Binkley, R. Seeger and J. A. Pople, *J. Chem. Phys.*, 1980, **72**, 650–654.
37 P. J. Hay and W. R. Wadt, *J. Chem. Phys.*, 1985, **82**, 270–283.
38 M. Okoshi, Y. Yamada, A. Yamada and H. Nakai, *J. Electrochem. Soc.*, 2013, **160**, A2160–A2165.
39 Z. Hu, C. Wang, C. Wang, B. Chen, C. Yang, S. Dong and G. Cui, *InfoMat*, 2022, **4**, e12249.
40 A. P. Thompson, H. M. Aktulga, R. Berger, D. S. Bolintineanu, W. M. Brown, P. S. Crozier, P. J. in 't

Veld, A. Kohlmeyer, S. G. Moore, T. D. Nguyen, R. Shan, M. J. Stevens, J. Tranchida, C. Trott and S. J. Plimpton, *Comput. Phys. Commun.*, 2022, **271**, 108171.

41 S. H. Lapidus, N. N. Rajput, X. Qu, K. W. Chapman, K. A. Persson and P. J. Chupas, *Phys. Chem. Chem. Phys.*, 2014, **16**, 21941–21945.

42 M. Callsen, K. Sodeyama, Z. Futera, Y. Tateyama and I. Hamada, *J. Phys. Chem. B*, 2017, **121**, 180–188.

43 C. I. Bayly, P. Cieplak, W. Cornell and P. A. Kollman, *J. Phys. Chem.*, 2002, **97**, 10269–10280.

44 R. W. Hockney and J. W. Eastwood, *Computer Simulation Using Particles*, 1988.